Environmental Science and Pollution Research (2023) 30:2740–2753
https://doi.org/10.1007/s11356-022-22049-1

RESEARCH ARTICLE

Photo–degradable and recyclable starch/Fe_3O_4/TiO_2 nanocomposites: feasibility of an approach to reduce the recycling labor cost in plastic waste management

Masoumeh Mohammadi-Alamuti[1] · Iman Shahabi-Ghahfarrokhi[1] · Maryam Shaterian[2]

Received: 6 May 2022 / Accepted: 12 July 2022 / Published online: 8 August 2022

Abstract

In this research, a biodegradable starch/Fe_3O_4/TiO_2 bio-nanocomposites (SFT) were produced using different nano Fe_3O_4/TiO_2 (FT) (3, 5, and 10 (wt% dry based)) contents. Mechanical properties, visual properties, moisture-sensitive parameters, magnetic properties, and physical properties of the film specimens were investigated. Photodegradability of film specimens was also evaluated under UV-A irradiation. The FT content increased the hydrophobicity of the film specimens. Tensile strength (TS) of SFT films was increased by increasing FT up to 3%. Elongation at break (EB) and tensile energy to break (TEB) were decreased by adding FT content up to 3% simultaneously. The film specimens' water vapor permeability (WVP) was decreased with increasing FT content. The intrinsic viscosity of SFT was decreased by increasing FT content. It confirms the enhancement of photodegradability of the specimens by increasing FT content. It seems the compatibility of FT with biopolymer has had great effects on these properties. Use of FT-based nanocomposites is an appropriate approach to developing magnetic-recyclable and photodegradable packaging materials.

Keywords Starch · Nano Fe_3O_4 · Nano TiO_2 · Automatic recycling · Eco-packaging

Introduction

Plastics have some properties, such as lightweight, transparent, and good mechanical properties. These properties have led to wide usage in different industries (Shrivastava 2018). In 2019, around 359 million tons of plastic were produced. While the amount of produced plastics has reached to 367 million tons in 2020 (Annonymous 2012).

The used plastics have three fates ahead, i.e., landfilling, burning, and recycling. The landfilled and abandoned plastics form microplastics in the environment and pollute the soil and water resources (Seymour 1989). However, burning the plastic wastes is an inexpensive energy resource, but some toxic pollutants produce during the process, i.e., acrolein, ketone, and methane (Briassoulis et al. 2004).

World plastic production in 2020 had been 367 million tons, which only 27.5 million tons of them were recycled (Annonymous 2012). Approximately, 21,000 workers are employed in US recycling industries who collect the recyclable wastes. Greenhouse gas (GHG) (2360 kg CO_2 eq) is emitted, and 39,664.1 MJ net energy value (diesel fuel and electricity) is consumed to produce 1 t of recycled plastics (Rosmiati 2020).

Plastic recycling is one of the approaches to deal with increasing plastic waste management. It can also be helpful to the management of petrochemical resources and energy saving. But, the high labor cost of plastic waste collection and sorting has approached uneconomically (Omrani 2005). On the other hand, in recycling plants, the labor forces face hazardous materials, e.g., used needles, dead animals, and broken glasses, which increase injury rates in recycling plants (Graham et al. 2015). After the COVID-19 pandemic, the health risks of the labor forces have been exacerbated.

For the past two decades, the development of biodegradable polymers and products from renewable resources have been considered a substitute for synthetic polymers

Responsible editor: George Z. Kyzas

✉ Iman Shahabi-Ghahfarrokhi
i.shahabi@znu.ac.ir

[1] Department of Food Science and Technology, Faculty of Agriculture, University of Zanjan, Zanjan 45371-38791, Iran

[2] Department of Chemistry, Faculty of Science, University of Zanjan, Zanjan 45371-38791, Iran

(Babaei-Ghazvini et al. 2018; Shahabi-Ghahfarrokhi et al. 2020). It is due to the non-renewable resources and the environmental pollution of synthetic plastics (Ashter 2016). However, the biopolymers, e.g., carbohydrates and proteins, are considered as food packaging materials because of their outstanding properties, i.e., impermeability against oxygen and carbon dioxide (Goudarzi et al. 2017; Hassannia-Kolaee et al. 2016; Zolfi et al. 2014). But, the biopolymer's drawbacks, i.e., weak mechanical properties, sensitivity to moisture, and lack of heat sealing, have been limited to their usage commercially (Shahabi-Ghahfarrokhi et al. 2015a). Among the biopolymers, starch is considered the best due to its abundance, availability, cost-effectiveness, and excellent film-forming ability (Ghanbarzadeh et al. 2010). Several modification methods have been applied to address the drawbacks of starch as packaging materials, e.g., composition with synthetic polymers (Tian et al. 2017) or biopolymers (Hassannia-Kolaee et al. 2016), nanoparticles (Ghanbarzadeh et al. 2010; Goudarzi et al. 2017; Hassannia-Kolaee et al. 2016; Shahabi-Ghahfarrokhi et al. 2015b), and ionizing rays (Goudarzi and Shahabi-Ghahfarrokhi 2018, Shahabi-Ghahfarrokhi and Babaei-Ghazvini 2019, Shahabi-Ghahfarrokhi et al. 2015a). Nevertheless, none of these drawbacks have been entirely resolved, and the packaging properties of the modified starch-based packaging materials are drastically weaker than the plastic ones.

Starch is a biodegradable polymer with the least side effects on the environment. Nevertheless, to produce 1 t of starch, the energy consumption (electricity and heat), the water consumption, and the total GHG emissions caused by fossil fuels are about 2527 MJ/t, 9.8 m^3/t, 539.8 kg CO_2 eq/t, respectively (Tran et al. 2015).

Fe_3O_4 (magnetite) is a magnetic particle with black color, low toxicity, and high surface area, which is easily separated under an external magnetic field. Therefore, Fe_3O_4 has been considered as a bioseparator in medical engineering and biomedical (Xu et al. 2014a). A reduction the particle size of magnetite can led to superparamagnetic properties. The superparamagnetic property of Fe_3O_4 nanoparticles can intensify the magnetic separation of the functional species, e.g., enzymes (Xu et al. 2014b) and drugs (Arruebo et al. 2007).

Titanium dioxide (TiO_2) is a high photostable, nontoxic, and inexpensive nanoparticle with white color which is used to develop nanocomposite packaging materials. TiO_2 is one of the most common photocatalysts which is used in the photocatalytic degradation process (Koysuren and Koysuren 2018). TiO_2 has a valence band with stable electrons and low energy and a conduction band that is empty. Band gap energy indicates the energy difference between the valence and conduction band, which is known as the least required photoenergy to redox reaction on the surface of TiO_2 during the photocatalytic process (Lee and Park 2013). TiO_2 absorbs the photon with more energy than band gap energy, e.g., UV ray.

Consequently, an electron is transmitted from the valence band to the conduction band, and an electron–hole pair due to photoexcitation is produced. These electron–hole pairs are transported on the photocatalyst surface, then react with adsorbed molecules on the photocatalyst surface such as water and oxygen, and finally make reactive oxygen species (ROS). ROS can degrade some organic pollutants through oxidation reactions (Zan et al. 2006). Moreover, TiO_2 can be used to intensify the photodegradation of polymers (Ali et al. 2016; Tu-morn et al. 2019) and biopolymers (Goudarzi and Shahabi-Ghahfarrokhi 2018). Coupling TiO_2 with transition metals, e.g., Fe_3O_4, can be reduced the band gap of TiO_2 and improves its photocatalytic activity at higher wavelengths of the electromagnetic spectrum (Carneiro et al. 2007).

The composition of TiO_2 and Fe_3O_4 as an enforcement agent in the matrix of biopolymers possesses several advantages in packaging materials. The white color of TiO_2 can mask the undesirable dark appearance of Fe_3O_4 in packaging materials. On the other hand, their simultaneous usage decreases the band gap energy in TiO_2 and intensifies the nanocomposites' photodegradation capability. Furthermore, the magnetic properties of Fe_3O_4 facilitate labor-free recycling of Fe_3O_4 nanocomposites. Accordingly, it seems this approach can be helpful in the development of labor-free recyclable packaging materials. Starch has been extensively investigated. Therefore, the excellent information about starch was an appropriate case study model for developing and investigating labor-free recyclable and photodegradable packaging materials.

Materials and methods

Materials

Corn starch (11–13% moisture) was purchased from Glucosan Co. (Qazvin, Iran). P25 TiO_2 nanoparticles with an average diameter of about 20 nm were supplied by US Research Nanomaterials, Inc. (Houston, USA). The analytic grade chemicals, including glycerol ($C_3H_8O_3$), iron(II) chloride ($FeCl_2$), sodium hydroxide (NaOH), and magnesium nitrite ($Mg(NO_2)_2$) were provided from Merck Co. (Darmstadt, Germany). Calcium chloride ($CaCl_2$) and sodium chloride (NaCl) were also supplied by Dr. Mojalali Co. (Tehran, Iran).

Preparation of Fe_3O_4 nanoparticles

Fe_3O_4 magnetic nanoparticles were prepared using the chemical co-precipitation method. Two grams of $FeCl_2$ was dissolved in distilled water (DW). The solution was then stirred at 60 °C using a heater stirrer. The solution was

passed through a cellulose filter, and 0.5 g of starch as a capping agent was added to the filtered solution to prevent further growth of the nanoparticles. Then, the solution was stirred at 60 ℃ until the solution was homogeneous. After that, NaOH solution (1 N) was added dropwise to the solution until the pH of the solution reached to 10. The solution was stirred for 1 h at 70–80 °C to precipitate magnetic nanoparticles. The suspension was centrifuged at 3000 RPM for 10 min to separate the Fe_3O_4 nanoparticles. Finally, in order to starch calcination, the precipitate was placed in a furnace (Pars Azma Co., Iran) at 500 °C for 1 h.

Preparation of film

Five percent (wt.%) starch solution was prepared in DW. The solution was then mixed and heated at 80 °C for 60 min to gelatinize the starch. Then, a plasticizer (glycerol, 40% wt.% of starch) was added to the film solution to make the film more flexible. After that, Fe_3O_4 and TiO_2 nanoparticles were mixed 1:1 and were dispersed by ultrasonic bath for 2–20-min intervals in DW. The homogenized suspension was added dropwise to the starch solution until the final FT content reached to 3%, 5%, and 10% (wt% of starch). Ultimately, 50 ml of the film-forming solution was cast on microbial plates with 15 cm diameter and dried at room temperature for 48 h.

Physical properties

Film thickness

The thickness of the film specimens was measured by a micrometer with an accuracy of 0.01 mm. The average thickness of samples at nine random positions was reported as film thickness.

Moisture content

Moisture content (MC) of the film specimens was determined in triplicate. In order to calculate the MC of film specimens, a certain amount of samples was weighed and dried by oven (Pars Azma Co., Iran) at 105 ± 1 °C up to constant weight. MC of film specimens was calculated according to Eq. 1.

$$MC = \frac{m_1 - m_2}{m_1} \times 100 \quad (1)$$

where m_1 is the weight of samples before drying in the oven, and m_2 is weight of samples after drying in the oven up to constant weight.

Moisture absorption

Moisture absorption (MA) of samples in three replicates was determined by the weight loss difference between film specimens which were conditioned at 0% RH (prepared by dry calcium chloride) and 55% RH (prepared by saturated magnesium nitrate solution). In order to measure MA of samples, the film specimens were cut into 2 cm × 2 cm pieces. Then, the samples were conditioned at 0% RH up to constant weight (m_3). After that, the samples were conditioned at RH of 55% at 25 °C up to constant weight (m_4). MA was calculated according to Eq. 2.

$$MA = \frac{m_4 - m_3}{m_3} \times 100 \quad (2)$$

Film solubility in water

Solubility in water (SW) was measured in triplicate to determine the amount of film substance that could be dissolved in DW. The film specimens were dried at 105 ± 1 °C to reach a constant weight (m_5). The dried film specimens were immersed in 50 ml DW and were stirred for 6 h at 25 °C. Afterward, the remaining film was separated from water and dried at 105 ± 1 °C to reach a constant weight (m_6). SW of samples was calculated according to Eq. 3.

$$SW = \frac{m_5 - m_6}{m_5} \times 100 \quad (3)$$

Water vapor permeability

Water vapor permeability (WVP) calculates the transfer of water molecules across the film specimens. WVP was measured in triplicate according to ASTM E96-95 (ASTM 1995). Glass vials were filled with dry calcium chloride to determine WVP. The glass vials were covered with the film specimens, and double-sided tape was used to seal the spout of the vial. After attaching the films to the vials, the vials were placed in a desiccator containing saturated sodium chloride with 75% RH. The vials were weighted with an accuracy of 0.0001 g at 1-h intervals. The linear regression model calculated the slope (S) of the time vs. weight. WVTR (Water vapor transmission rate) and WVP of specimens were calculated according to Eqs. 4 and 5, respectively.

$$WVTR = \frac{S}{A} \quad (4)$$

$$WVP = \frac{WVTR \times X}{\Delta P} \quad (5)$$

where A is the effective film area (m^2), X is the average film thickness (m), and ΔP is the difference in vapor pressure on both sides of the film (1753.55 Pa).

Colorimetric measurements

The color of film specimens was measured using a portable colorimeter (TES 135, Electronic Corp., Taiwan). The samples were measured in triplicate. The white standard plate (L^* = 94.57, a^* = -4.87, b^* = -2.168) was used as the background for film specimens. The total color difference (ΔE), whiteness index (WI), yellowness index (YI), and browning index (BI) were calculated according to Eqs. 6, 7, 8, and 9, respectively (Djekic et al. 2017, Goudarzi and Shahabi-Ghahfarrokhi 2018).

$$\Delta E = \sqrt{(L^* - L)^2 + (a^* - a)^2 + (b^* - b)^2} \quad (6)$$

$$WI = 100 - \sqrt{(100 - L)^2 + a^2 + b^2} \quad (7)$$

$$YI = \frac{142.86 \times b}{L} \quad (8)$$

$$BI = \frac{100\left(\frac{a+1.75L}{5.645L+a-3.012b} - 0.31\right)}{0.172} \quad (9)$$

Mechanical properties

The mechanical properties of film specimens were measured according to ASTM standard method D882-02 (ASTM 2002) with some modifications by a mechanical evaluation device (STM-5, Santam Co, Iran). The ribbon films (width of 10 mm and length of 100 mm) were conditioned at a desiccator containing saturated magnesium nitrate solution with 50 to 55% RH for at least 48 h. The initial grip separation and the rate of grip separation were set at 60 mm and 10 mm/min, respectively. TS, EB, and TEB were calculated for film specimens according to Eqs. 10, 11, and 12, respectively.

$$TS(MPa) = \frac{F_{max}}{A_{min}} \quad (10)$$

$$EB(\%) = \frac{L_{max}}{L_0} \quad (11)$$

$$TEB(MPa) = \int_0^{\varepsilon} S d\varepsilon \quad (12)$$

where F_{max} is the maximum force (N), A_{min} is the minimum cross-sectional area (mm^2), L_{max} is the extension at the moment of rupture (mm), L_0 is the initial grip separation (mm), S is the stress at any strain,ε is the strain at rupture.

Microstructural

Field emission scanning electron microscope (FE-SEM) (TESCAN, MIRA3, Czech Republic) was used to investigate the microstructure of the surface and cross section of the film specimens and the nanoparticles. The samples were fractured in liquid nitrogen to examine the cross section of the specimens. Afterward, the mounted specimens on aluminum stubs were sputtered by gold for 5 min. The samples were observed with an accelerating voltage of 5 kV with different magnifications.

Contact angle

The contact angle of film specimens was measured by the sessile drop method, which is a standard method for determining surface wettability. To measure the contact angle according to this method, a drop of water was placed on the surface of film specimens, and its image was captured by a digital camera (AM2111, Dino light, Taiwan). The contact angle plugin in ImageJ software (version Java 1.8.0_172) was used to calculate the contact angle of the water droplet with the film surface.

UV–Vis spectroscopy

The UV–Vis spectrum of the film specimens was obtained by spectrophotometer (SPECORD 250 UV/VIS, Germany) in the range of 190 to 800 nm. The empty quartz cuvette (EQC) was considered as a baseline. The film specimens were fixed between EQC and the sample holder. Then the samples were scanned in the UV–Vis range.

Density of films

The density of film specimens was determined in triplicate according to ISO standard 1183–1 by pycnometer method (ISO 2019) and some modifications. The density of a film specimen (ρ_s) is the mass per unit volume of a sample at 20 °C. The density of the film specimens was measured by a dry, clean and empty pycnometer weighted (W_p). The pycnometer and a few pieces of film were weighted (W_{ps}). Then, the pycnometer containing the film pieces was filled with a proper solvent (n-hexane) and weighted (W_{pls}). The dry, clean, empty pycnometer was filled with n-hexane and weighted (W_{pl}). Finally, the dry, clean, empty pycnometer was filled with DW and weighted (W_{pw}). The ambient, film, and solvents temperature was 20 °C. Density of DW (ρ_w) at

20 °C is 0.9982 g/cm^3. Density of the specimens was calculated according to Eqs. 13, 14, and 15.

$$\rho_l = \frac{(w_{pl} - w_p) \times \rho_w}{(w_{pw} - w_p)} \quad (13)$$

$$V_s = \frac{(W_{pl} - W_p) - (W_{pls} - W_{ps})}{\rho_l} \quad (14)$$

$$\rho_s = w_s / v_s \quad (15)$$

Photodegradation evaluation

To investigate the photodegradation of film specimens, the specimens were exposed to UV-A (3 × 8 W) lamps for 10 days. Then, the intrinsic viscosity of the films was determined after 2, 5, and 10 days of UV-A curing. The film specimens were dissolved in NaOH 0.4 N by heating. The intrinsic viscosity was measured using a Cannon–Fenske Routine viscometer at 20 °C. The intrinsic viscosity of specimens was determined by the Huggins (Eq. 16) and Kraemer (Eq. 17) equations, respectively (Shahabi-Ghahfarrokhi et al. 2015a).

$$\frac{\eta_{SP}}{C} = [\eta] + K_H[\eta]^2 C \quad (16)$$

$$\frac{\ln(\eta_{rel})}{C} = [\eta] + K_K + [\eta]^2 C \quad (17)$$

where $[\eta]$, η_{SP}, and η_{rel} are intrinsic viscosity, specific viscosity, and relative viscosity, respectively. K_H and K_K are the Huggins and Kraemer coefficients, respectively. C is the concentration of the film solutions in NaOH 0.4 N. η_{SP} and η_{rel} were calculated by Eqs. 18 and 19, respectively.

$$\eta_{rel} = t_{stu} / t_{stv} \quad (18)$$

$$\eta_{SP} = \eta_{rel} - 1 \quad (19)$$

where t_{slu} and t_{slv} are average efflux time of NaOH 0.4 N and solution of the film solutions in NaOH 0.4 N, respectively.

The photodegradation rate (PDR) of film specimens during UV-A exposure (0, 2, 5, and 10 days) was calculated according to (Eq. 20). The PDR was calculated based on the change rate of intrinsic viscosity of a sample during UV-A curing intervals (0, 2, 5, and 10 days).

$$PDR_i = \frac{[\eta]_i - [\eta]_{i-t}}{[\eta]_{i-t}} \times 100 \quad (20)$$

where $[\eta]_i$ is intrinsic viscosity of film specimen at a UV curing time (i = 2, 5, and 10 days), and $[\eta]_{i-t}$ is intrinsic viscosity of film specimen in a previous UV curing time (i-t = 0, 2, and 5 days). For example, the intrinsic viscosity of the film at 5th day ($[\eta]_5$) and the intrinsic viscosity of the film at 2nd day ($[\eta]_2$) were used to calculate PDR after 5 days (PDR_5).

Magnetic properties

Magnetic properties of film specimens were performed in a VSM (Magnetic Daghigh Kavir, MDKB, Iran) at room temperature. The applied field on the samples was in the parallel direction, and the range of applied field was between − 20,000 and + 20,000 Oe.

Statistical analysis

The statistical design of this study was performed in a completely randomized design and analyzed by ANOVA method using SPSS software (Version 26; SPSS Inc., USA), and the means were compared by Duncan method at the probability level of 0.05.

Results and discussion

Visual properties

The visual properties of starch and SFT bio-nanocomposites are shown in Fig. 1. As shown, the dark color of Fe_3O_4 nanoparticles has intensified the dark color of FT and has decreased the transparency of film specimens. It is obvious that with increasing FT content, the color of films becomes darker (Fig. 1).

Fig. 1 Visual properties of the starch (**a**) and starch/ Fe_3O_4/TiO_2 nanocomposite films with different Fe_3O_4/TiO_2 content 3% (**b**), 5% (**c**), 10% (**d**) with backlight

Color

One of the duties of food packaging, in addition to protection of the packaging content is creation of a communication cover to attract the customers. Therefore, the color, transparency, and appearance of packaging are the essential parameters that should be considered. Table 1 shows the parameters of *L*, *a*, *b*,ΔE, WI, YI, and BI. All the color parameters depend on the content of FT. With increasing FT content, *L* and WI values were decreased, and *a*, *b*,ΔE, YI, and BI values were increased simultaneously. The visual properties of bio-nanocomposites depend on the visual properties of biopolymers and nanoparticles and the size of nanoparticles (Caseri 2010; Goudarzi et al. 2017). However, some of the metallic nanoparticles (e.g., ZnO) have no side effects on the visual properties of the nanocomposites (Shahabi-Ghahfarrokhi et al. 2015c). But the others (e.g., TiO_2, Fe_3O_4) have drastic changes in visual properties (Chen et al. 2018, Goudarzi and Shahabi-Ghahfarrokhi 2018, Goudarzi et al. 2017).

UV–Vis spectrum

The transmission of UV (100–400 nm) and visible (400–750 nm) spectra across the packaging materials is an important parameter to improve the aesthetic properties of packaging and protect the packaging content against photochemical spoilage. The formation of free radicals, antioxidant destruction, lipid oxidation, nutrient degradation, discoloration, and off-flavor by UV ray accelerate foods spoilage (Kim et al. 2019).

The UV–Vis spectra of starch and SFT are shown in Fig. 2. The UV–Vis absorption of SFTs was drastically higher than the UV–Vis absorption of starch. The difference between visible spectra of starch and SFTs agreed with the visual properties of the samples (Fig. 1a). The absorption of the visible spectra was increased with increasing FT content. However, the absorption spectra of all the samples were augmented with decreasing the wavelength because of conjugated double bonds in the chemical structure of starch. But the absorption of SFTs was significantly higher than

Table 1 Hunter color values (*L*, *a*, and *b*), total color difference (Δ*E*), whiteness index (WI), yellowness index (YI), and browning index (BI) of starch and starch/Fe_3O_4/TiO_2 nanocomposite films with different Fe_3O_4/TiO_2 content

Fe_3O_4/TiO_2 content (%)	*L*	*A*	*b*	ΔE	WI	YI	BI
0	90.61 ± 0.96a	− 4.48 ± 0.56d	− 0.67 ± 0.52c	4.30 ± 0.95d	89.54 ± 0.70a	− 1.05 ± 0.81c	− 4.23 ± 0.46c
3	75.60 ± 0.64b	1.13 ± 0.56c	7.20 ± 0.85b	22.01 ± 1.05c	74.52 ± 0.86b	13.69 ± 1.71b	10.82 ± 1.82b
5	69.58 ± 2.37c	2.40 ± 0.60b	8.38 ± 0.55b	27.88 ± 2.33b	68.58 ± 2.40c	17.17 ± 1.60b	14.89 ± 1.50b
10	53.2 ± 1.18d	8.51 ± 0.50a	10.83 ± 0.20a	45.38 ± 1.16a	51.21 ± 1.18d	29.08 ± 0.84a	33.66 ± 1.19a

Means within each column with the same letters are not significant ($P < 0.05$). Data are means ± SD

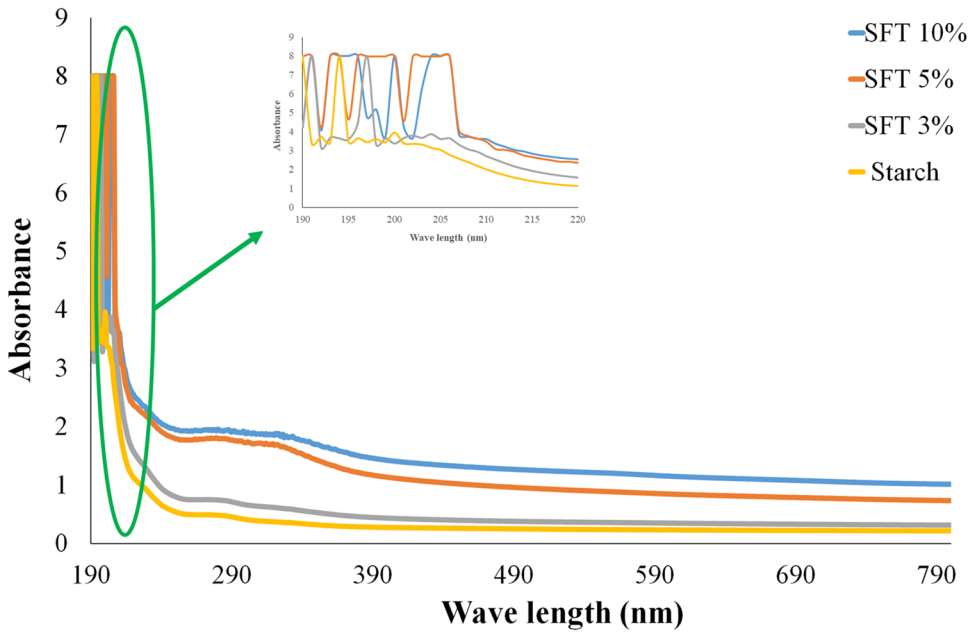

Fig. 2 UV–Vis absorption spectra of starch and starch/Fe_3O_4/TiO_2 nanocomposite films with different Fe3O4/TiO2 content 3% (SFT 3%), 5% (SFT 5%), 10% (SFT 10%)

starch in this range. The peak intensity has been observed in TiO_2 (Goudarzi et al. 2017, Wang and Zhang 2011), ZnO (Shahabi-Ghahfarrokhi and Babaei-Ghazvini 2019, Shahabi-Ghahfarrokhi et al. 2015c), and Fe_3O_4 (Ding et al. 2015) based nanocomposites. It confirms the UV-protective properties of the SFT films.

Microstructure

The size and shape of the prepared Fe_3O_4 nanoparticles is illustrated in Fig. 3 (N). Fe_3O_4 nanoparticles are spherical with an average diameter 71 ± 4 nm. Figure 3 shows the SEM images of the surface and cross section of film specimens. The surface of the starch film was uniform and smooth. This appearance was observed in SFT 3%. It confirms the homogenous dispersion of FT in the matrix of starch. While with increasing FT content (5% and 10%), FT was not well dispersed in the starch matrix, and some aggregated FT particles were observed. It shows the inappropriate compatibility of FT with the matrix of starch at higher FT contents. It seems the aggregation of FT has been due to the high surface energy of FTs and Van der Waals interaction between them (Goudarzi et al. 2017; Shahabi-Ghahfarrokhi et al. 2015c).

The cross section of starch and SFT are shown in Fig. 3. There are some microcracks in the cross section of the starch and SFT films. The cross section of starch is smoother than SFTs. However, there is no clear aggregated FT in SFT 3%. But FT was aggregated clearly in SFT 5% and 10%. This phenomenon has been observed in other bio-nanocomposites (Goudarzi et al. 2017; Shahabi-Ghahfarrokhi et al. 2015c). It seems it depends on the biopolymer and nanoparticle type, preparation method, and performed modification in biopolymer and nanoparticle (Goudarzi et al. 2017; Shahabi-Ghahfarrokhi et al. 2015c).

Density of film specimens

The density of film specimens is shown in Table 3. The density of the film specimens was increased up to FT 3%. In comparison, SEM micrographs (Fig. 3) show more homogenous and compact microstructures in the cross section of starch film than SFT 3%. It seems that the increase in SFT (3%) density was due to the high density of Fe_3O_4 (5.2 g/cm^3) and TiO_2 (4.23 g/cm^3). On the other hand, density of SFT (5% and 10%) decreased significantly. It was independent of FT content but was more than starch film. As shown in Fig. 3, reducing the density was due to increasing the free

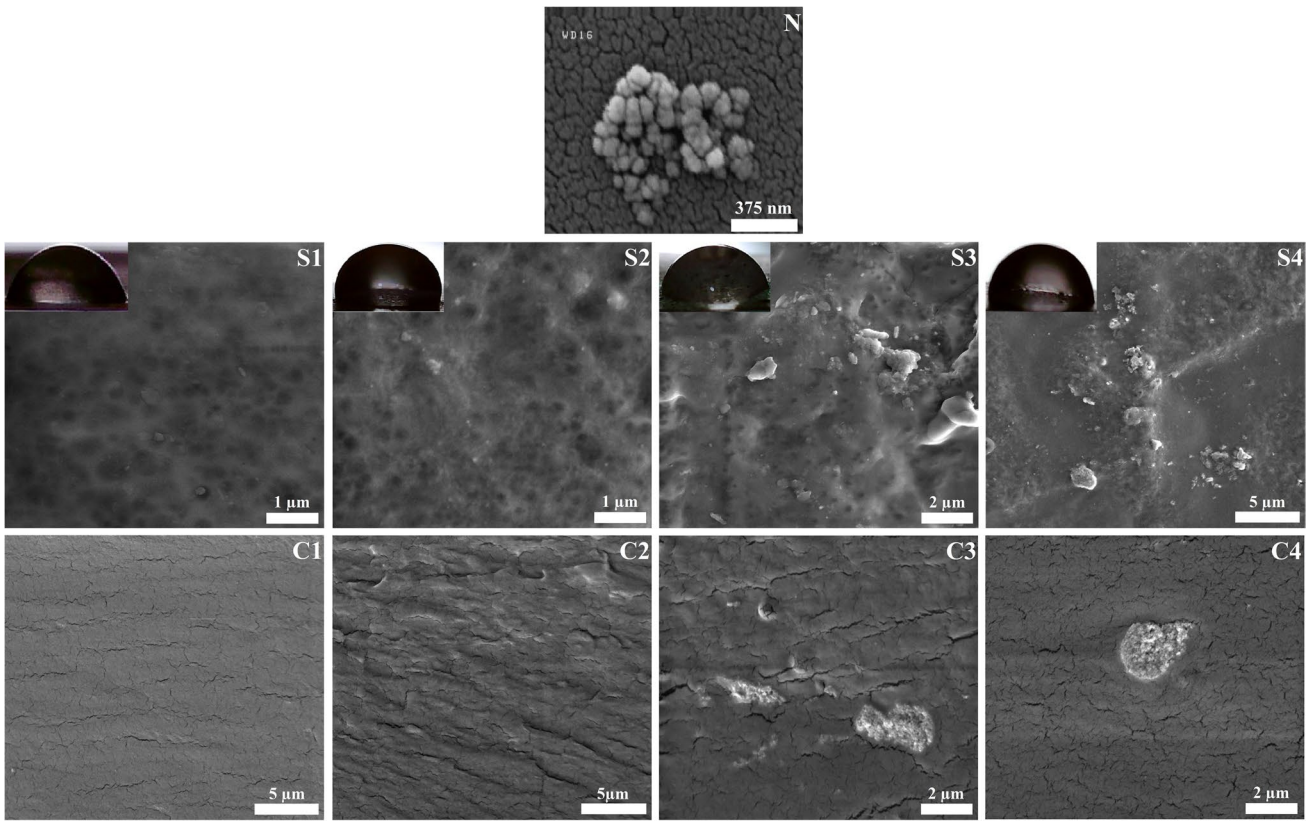

Fig. 3 Scanning electron micrographs of surface (S) and cross section (C) of (1) starch, (2) starch/Fe_3O_4/TiO_2 (3%), (3) starch/Fe_3O_4/TiO_2 (5%), (4) starch/Fe_3O_4/TiO_2 (10%). (N) SEM of Fe_3O_4 nanoparticles

spaces around the aggregated FT and porous microstructure of the biopolymer matrix. Despite the positive effect of Fe_3O_4 and TiO_2 density on SFT density at high FT content (5% and 10%), the free spaces' countervailing influence in SFT films (Fig. 3) depredates the increasing of the density.

Contact angle

Measuring the contact angle is an excellent approach to determining the hydrophobicity and hydrophilicity of the surface. When the water spreads over the surface without the formation of droplets, the surface is called hydrophilic, while the form of water droplets with high contact angle confirms the hydrophobic surface. Contact angle measurement is a simple and quantitative method for determining water droplet interactions on a solid surface. Practically, hydrophobicity and hydrophilicity are relative terms. Surface with water contact angles less than 90° are considered hydrophilic, and surface with contact angles greater than 90° are considered hydrophobic (Arkles 2006).

To determine the contact angle on a real surface, two models, i.e., the Wenzel model and Cassie-Baxter model, are developed. The real surfaces have chemical heterogeneity and surface roughness compared with the ideal surface. The contact angle of a rough surface with chemical homogeneity is considered by Wenzel model (Wenzel 1936). In comparison, the wettability of the flat surface with chemical heterogeneity is considered by the Cassie-Baxter model (Cassie and Baxter 1944). According to the Wenzel model, it can be concluded that the surface roughness intensifies the hydrophilic and hydrophobic properties of the original surface. From the Cassie-Baxter model, it can be deduced that the area fractions under the drop are essential in that the more significant the area fraction of air, the higher the contact angle (Seo and Kim 2015). Concerning Wenzel and Cassie-Baxter's model, the contact angle of the solid surface depends on the surface's chemical homogeneity, hydrophobicity, and roughness.

Table 2 shows the results of the contact angle of film specimens. The contact angle of the film specimens was increased up to SFT 3%. After that, the contact angle of SFT (5% and 10%) decreased significantly. As shown in Fig. 3 (S1–S4), the surface of the films was roughened by increasing FT. As mentioned, the surface roughness leads to increasing the contact angle. It seems that the homogenous distribution of FT in SFT 3% has created a homogeneous rough surface. Furthermore, the formed hydrogen bonds between oxygen in Fe_3O_4 and TiO_2 restrain forming appropriate bonds between the water droplet and the surface (Goudarzi et al. 2017, Shahabi-Ghahfarrokhi and Babaei-Ghazvini 2019). Consequently, the contact angle was increased significantly.

But at higher FT content (5% and 10%), however, the aggregated FT formed a rougher surface on SFT, but the inappropriate distribution of FT increased the free hydrophilic sites of the surface. Consequently, the contact angle decreased after SFT by 3%. A similar result has been reported (Goudarzi et al. 2017). But there are contradictory results in this field (Kim et al. 2019). The contradiction is due to the type of biopolymers, nanoparticles, and the preparation method of films.

Thickness

As shown in Table 2, the thickness of film specimens was independent of FT content. The thickness of the different nanocomposites changes dependently or independently with changes in nanoparticles content and biopolymer (Goudarzi et al. 2017, Salarbashi et al. 2016, Shahabi-Ghahfarrokhi and Babaei-Ghazvini 2019). It seems, the contradiction depends on the film preparation method, the type of nanoparticles, and the biopolymers.

Sensitivity to moisture

One of the main limitations of biopolymers in food packaging is their sensitivity to water. So, many researchers have been attempted to improve the moisture sensitivity of biopolymers. (Goudarzi and Shahabi-Ghahfarrokhi 2018, Goudarzi et al. 2017, Hassannia-Kolaee et al. 2016, Salarbashi et al. 2016). MC, MA, and SW of film specimens are shown in Table 2. SW was independent of FT content. MC and MA of SFT film were decreased with increasing FT content. It seems that increasing the structure density, the hydrophobic

Table 2 Physical properties, contact angle, and density of starch/Fe_3O_4/TiO_2 nanocomposites incorporated with different Fe_3O_4/ TiO_2 content

Fe_3O_4/TiO_2 content (%)	Thickness (mm)	Moisture content (%)	Moisture absorption (%)	Solubility in water (%)	Density (g/cm^3)	Contact angle (°)
0	0.08 ± 0.01a	20.49 ± 0.99a	10.06 ± 0.33a	15.80 ± 0.91a	0.78 ± 0.01c	76.59 ± 2.17d
3	0.09 ± 0.02a	18.11 ± 0.74a	9.35 ± 0.71b	15.07 ± 0.42a	0.94 ± 0.00a	101.53 ± 2.80a
5	0.10 ± 0.01a	16.41 ± 0.13b	9.30 ± 0.23b	14.98 ± 1.21a	0.86 ± 0.04b	95.34 ± 2.47c
10	0.10 ± 0.00a	12.87 ± 1.47c	8.54 ± 0.01c	15.10 ± 0.46a	0.87 ± 0.05b	97.37 ± 1.28b

Means within each column with the same letters are not significantly ($P < 0.05$). Data are means ± SD

properties, and the formed hydrogen bonds between starch and FT nanoparticles were the main factors in this phenomena (Goudarzi and Shahabi-Ghahfarrokhi 2018, Shahabi-Ghahfarrokhi et al. 2015c). Furthermore, the sensitivity of nanocomposites to moisture depends on the type of biopolymers, the type of nanoparticles, and the film preparation methods (Goudarzi et al. 2017).

Water vapor permeability

WVP is a crucial property in food packaging. The poor barrier properties of packaging materials lead to quick moisture exchange between food products and ambient humidity. Lower WVP values indicate better moisture barrier properties. Appropriate WVP can be guaranteed to improve the storage, transportation, and prolong shelf life span of the product (Gaikwad 2015).

Table 3 shows the WVP values of film specimens. WVP of the films was decreased by increasing FT content. WVP of the bio-nanocomposites up to 5% were independent of FT content. As shown in Fig. 3 (C1–C4), there were many microcracks in the cross section of all the film specimens. But the microcracks of the starch film were homogeneously dispersed. While by adding 3% of FT nanoparticles to the starch matrix, the microcracks were decreased. This could be related to the excellent compatibility of the nanoparticles in the low level (3%) with starch matrix, which is due to the formed hydrogen bonds (Almasi et al. 2010; Goudarzi et al. 2017; Shahabi-Ghahfarrokhi et al. 2015c; Zhou et al. 2009) between starch and FT.

Consequently, the structural density was increased (Table 2) and led to a tortuous path to moisture transition (Hassannia-Kolaee et al. 2016, Kristo and Biliaderis 2007) as well as some aggregated FTs appeared in high FT content (5% and 10%) films. The aggregated FTs formed a barrier across the SFT films (Chau et al. 2009). The free spaces may be formed around aggregated nanoparticles and increased WVP of nanocomposites (Jamróz et al. 2019). Nevertheless, It seems the formed hydrogen bounds (Almasi et al. 2010; Goudarzi et al. 2017; Shahabi-Ghahfarrokhi et al. 2015c; Zhou et al. 2009), the formed impermeable aggregated FTs, the formed tortuous path to moisture transition (Hassannia-Kolaee et al. 2016, Kristo &Biliaderis 2007), and/or unknown factors effectively decreased WVP of SFTs by increasing FT content.

Mechanical properties

The mechanical properties of food packaging are essential in machine performance and protect package content against various stresses during processing and transportation. So, determining the mechanical properties of food packaging is one of the essential characteristics that should be evaluated. Mechanical properties were determined by assessing TS, EB, and TEB. TS indicates the maximum load that a material can withstand before it breaks or tears. EB indicates the flexibility or the extension capacity of films before fracture. TEB or toughness suggests the total absorbed energy per unit volume of the specimen up to rupture point (ASTM 2002).

Table 3 shows the mechanical properties of film specimens. TS of film specimens was increased significantly by increasing FT content up to 3%. After that, TS decreased drastically at high FT content (5% and 10%). So that it was lower than starch film. There is a good correlation between micrographs (Fig. 3) and mechanical properties. There are several microcracks which have distributed homogenously in starch film. The number of microcracks was decreased by increasing FT content up to 3% and, after that, several heterogeneous microcracks were formed and FTs were aggregated at high FT content (5% and 10%). It seems that the tensile force has focused on the microcracks and the aggregated FT. Consequently, the films were ruptured in the focused force points.

EB and TEB of the SFT were decreased up to 3% FT content. After that, they increased drastically. It seems that the formed hydrogen bonds between FT and starch matrix have restricted the movements of starch chains (Müller et al. 2011; Salarbashi et al. 2017). On the other hand, due to the low affinity between the nanoparticles and the matrix of the biopolymer, the aggregated FT facilitated the movement of starch chains like a ball bearing system (Goudarzi et al. 2017). EB and TEB were increased significantly with increasing FT content (5% and 10%). There is a good agreement with previous study (Salarbashi et al. 2017).

Table 3 Fe_3O_4/TiO_2 content affects the mechanical properties of starch and starch/Fe_3O_4/TiO_2 with different Fe_3o_4/TiO_2 content

Fe_3O_4/TiO_2 content (%)	Tensile strength (MPa)	Elongation at break (%)	Tensile energy to break (MJ/m^3)	WVP ($\times 10^{-10}$ $gm^{-1}s^{-1}Pa^{-1}$)
0	8.01 ± 0.01b	36.59 ± 0.44a	2.93 ± 0.59a	4.86 ± 0.69a
3	9.67 ± 0.82a	30.70 ± 0.75b	1.41 ± 0.38b	4.27 ± 0.61ab
5	7.03 ± 0.41c	40.68 ± 4.48a	2.79 ± 0.54a	4.17 ± 0.02ab
10	6.87 ± 0.32c	39.98 ± 3.93a	2.55 ± 0.03a	3.47 ± 0.46b

Means within each column with the same letters are not significant ($P < 0.05$). Data are means ± SD

Photodegradation and its mechanism

Photodegradation is the alteration of materials by light; the term refers to the combined sunlight and air for oxidation and hydrolysis of some substrates. UV spectrum of the sunlight increases photodegradation compare to the visible spectrum. Forasmuch as the biodegradation of polymers by conventional methods is very difficult. While the solid-phase photocatalytic process is an ideal method for the degradation of polymer wastes using sustainable solar energy (Xing et al. 2016).

The formed free-radicals during UV exposer, degrade many environmental pollutants and polymers by photooxidation and breaking down polymers chains. These changes after an unpredictable period, cause weak mechanical properties, low molecular weight polymers and produce useless materials (Yousif and Haddad 2013). UV radiation consists about 5% of sun light. However, UV-B is more efficient for investigating photodegradability of polymers. But more than 95% of the sun UV light is UV-A. As well as the leakage of UV-A is more than UV-B from ozone layer (Annonymous 2012). Therefore, UV-A is considered to investigate photodegradation of SFT.

Photochemical activities of TiO_2 and other semiconductors are associated with two types of electron bands: a filled low energy band, which is called the valence band, and an empty high energy band, which is called the conduction band. The movement of electrons between these two bands is the main factor in performing photochemical reactions. There is an energy difference between two energy bands which is called band gap (Koysuren and Koysuren 2018).

UV radiating to the surface of TiO_2 leads to form photoelectrons and photoholes on it. These photoelectrons and photoholes react with the moisture and oxygen in the environment and lead to the production of reactive oxygen species (ROS) (Fig. 4a). Consequently, the produced free electrons and superoxide radicals lead to the polymer chains' destruction and accelerate the chain fracture (Zan et al. 2006). The relatively high band gap in TiO_2 limits its photochemical activities to UV wavelength. TiO_2 doping with transition metals is an approach to overcome with this defect. Because of creation some impurity energy levels within the valence band and conduction band of TiO_2 by transition metals (Fig. 4a). So, TiO_2 can be activated at higher wavelengths. Hence, some metals such as Fe_3O_4 can be used to dope TiO_2 nanoparticles for narrowing the band gap, enhancing the photodegradation by the visible wavelength, and enhancing the photodegradation (George et al. 2011).

The intrinsic viscosity indicates the occupied hydrodynamic volume by the polymer in a solution. (Shahabi-Ghahfarrokhi et al. 2015a). It is well known that there is a direct relationship between the molecular weight and intrinsic viscosity of polymer solution. Therefore, decreasing the intrinsic viscosity confirms the reduction of the molecular weight of the polymer. This phenomenon indicates the breakdown of the polymer chain during degradation. Table 4 shows the intrinsic viscosity of starch and SFT films. The intrinsic viscosity of the film specimens was decreased significantly with increasing UV-A exposure time. On the other hand, with increasing FT content, the film specimens' intrinsic viscosity was reduced, significantly (Bohdanecky and Kavar 1982). It seems that UV-A ray with FT accompaniment have led to break starch chains (Fig. 4b) and decrease their

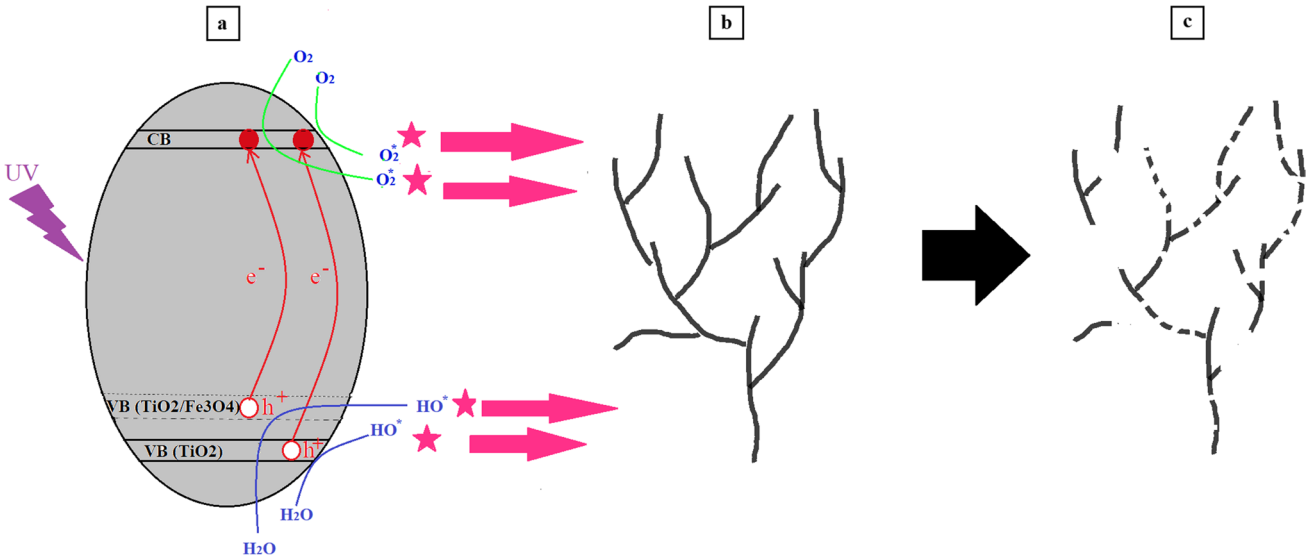

Fig. 4 Photodegradation mechanism of starch/Fe_3O_4/TiO_2 bio-nanocomposites under UV-ray: (**a**) free radical production by electron–hole mechanism on Fe_3O_4/TiO_2 under UV-ray, (**b**) virgin starch, (**c**) degraded starch by photodegradation

Table 4 Intrinsic viscosity of starch and starch based nanocomposite with different Fe_3O_4/TiO_2 content, 3% (SFT 3),5% (SFT 5), and 10% (SFT 10) during 10-day UV-A exposure

Time (day)	Starch	SFT3	SFT5	SFT10
0	15.64 ± 0.02ae	15.32 ± 0.04af	14.91 ± 0.10ag	14.79 ± 0.19ah
2	14.24 ± 0.07be	12.05 ± 0.15bf	11.73 ± 0.08bg	10.46 ± 0.10bh
5	9.40 ± 0.05ce	9.24 ± 0.05ce	7.84 ± 0.13cf	7.22 ± 0.02cf
10	8.93 ± 0.09de	8.51 ± 0.31df	7.31 ± 0.19dg	6.38 ± 0.10dh

Means within each column with the same letters (a–d) are not significantly different ($P < 0.05$). Means within each raw with the same letters (e–h) are not significantly different ($P < 0.05$). Data are means ± SD

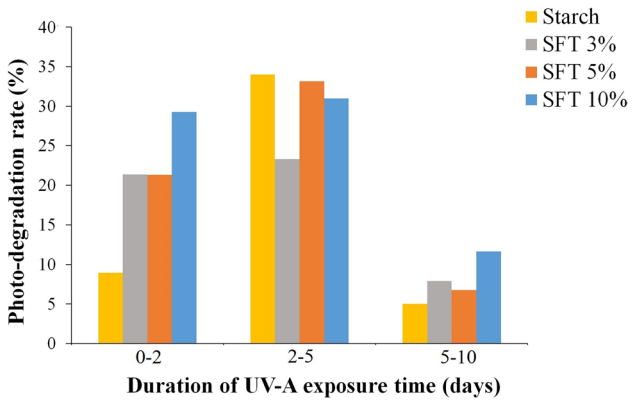

Fig. 5 Photodegradation rate of starch and starch/Fe_3O_4/TiO_2 nanocomposite films with different Fe_3O_4/TiO_2 content 3% (SFT 3%), 5% (SFT 5%), 10% (SFT 10%)

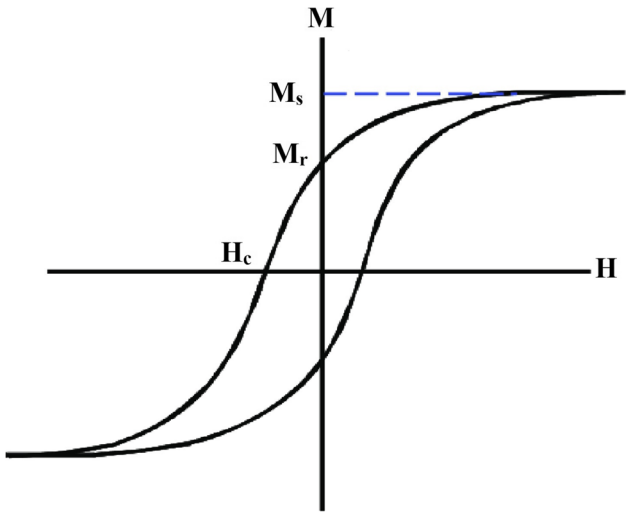

Fig. 6 Magnetic hysteresis loop (Billings et al. 2009)

molecular weight (Fig. 4c). The numbers of ROS increase with increasing the content of photoactive nanoparticles and UV exposure time which intensify the photodegradation of the specimens(Cho and Choi 2001, Goudarzi and Shahabi-Ghahfarrokhi 2018, Nakayama and Hayashi 2007).

Figure 5 shows the PDR of starch film and SFTs (3%, 5%, and 10%) at different UV-A exposure timespan (0–2, 2–5, 5–10 days). The PDR of the samples was increased up to 5 days. After that, PDR of the samples decreased up to 10 days, significantly. It seems the amorphous parts of the starch chains were degraded after 5 days, and reminded the resistant parts of the starch chain, which has decreased in PDR after that. PDR of SFTs was higher than starch at all times except at 2–5 timespan. It seems that the absence of FT has decreased ROS formation under UV exposure. Consequently, degradation of the amorphous was delayed up to 2–5 timespan as well, and PDR of SFTs was increased with increasing FT content which confirmed this phenomenon in the SFTs.

Magnetic properties

Magnetic properties of the material are considered in a wide range of industries. Magnet has long been used as an appropriate approach to separate magnetic-metal scraps from municipal waste to increase the separation speed and accuracy while also reducing the labor cost of separation. Despite the increase in plastic waste recycling rates in the last decade, only less than 10% is recycled (Anonymous 2018). The high labor cost of plastic recycling is one of the main factors of this defect. VSM is considered a common instrument to measure the magnetic properties of materials. The source of magnetic properties in solids is mobile electrons. Determining the relative magnetic orientation of electrons in an ion depends on the interactions between the electrons (Thompson and Oldfield 1986).

Figure 6 shows the magnetic hysteresis loop of magnetic particles. When a ferromagnetic material, e.g. iron, is exposed to a magnetic field, its torques are aligned with the field. When all its torques are aligned with the field, magnetization reaches a state of saturation, so-called saturation magnetization (M_s). If the applied field decreases, several torques deviate from the applied field, and some of them remain in the direction of the area, which is called remnant magnetization (M_r), which indicates the magnetic induction remaining in the solid. If the applied field decreases to coercive force (H_c), the magnetic induction decreases to zero. H_c is the amount of field required to reduce the magnetization caused by the applied field to zero. By lowering the applied field, magnetization reaches saturation magnetization

again, and by repeating the above states, a hysteresis loop is obtained, called a magnetic hysteresis loop.

Due to its narrow magnetic hysteresis loop, soft ferromagnetic materials such as irons have minimal amounts of residual magnetism. Therefore, they can be magnetized and demagnetized, easily. However, the hard magnetic materials have wide hysteresis loops; these materials are not easily magnetized, and larger magnetic fields are required to magnetize them. Hard magnetic materials have higher retentivity and coercivity (Dresselhaus 1999).

Figure 7 shows the magnetic hysteresis loop of film specimens. M_s and M_r were increased with increasing the FT content. As shown, the film specimens have low coercive force. Therefore, magnetic films have a soft ferromagnetic behavior (Nayak 2006). Soft magnetic materials are easily magnetized by applying a small magnetic field, and by reducing the applied field up to zero, they quickly lose their torque. These materials also have high saturation magnetization and low remnant magnetization.

Conclusion

The environmental pollution of plastic-based packaging and the low plastic recycling rate has led to bioplastics' development in the last two decades. The drawbacks of the bioplastics have been restricted the bioplastic's usage in food packaging. On the other hand, the high labor cost of the recycling system persuades us to develop a photodegradable and labor-free recyclable packaging material.

The characterization of the SFT films confirmed the reinforcement of mechanical properties of starched-based packaging material by FT. Furthermore, the moisture sensitivity and moisture barriers of starch-based packaging materials were resolved by FT. On the other hand, SFT film can be filtered by UV ray and protect the content against photospoilage. The magnetic properties of SFT films confirmed the soft ferromagnetic behavior in the SFT films. Therefore, the magnet can easily absorb SFT films (Video 1).

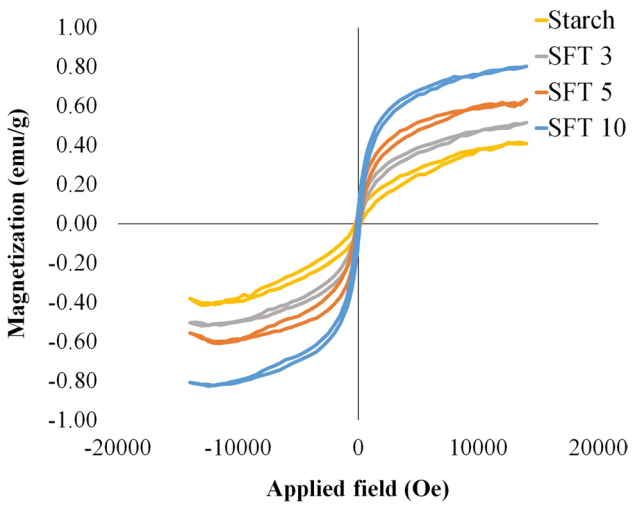

Fig. 7 Hysteresis loops of starch and starch based nanoparticle with different Fe_3O_4/TiO_2 content, 3% (SFT3), 5% (SFT5), and 10% (SFT10)

Consequently, the FT-based nanocomposites can be recycled automatically by the usual magnets in the recycling system of municipal waste. If the FT-based plastics are not recycled, they can be degraded rapidly compared to virgin polymers. The formed microplastics by FT-based nanocomposite can be easily recycled from the environment and reduce their risks.

However, in the current study, starch-based packaging material was considered only a case study with easy, low-cost preparation, and fast photodegradation process. But this approach is performable in starch-based packaging material and can be used to develop a labor-free recycling system for petroleum-based plastics. Nevertheless, this approach does not apply to all packaging materials due to the side effect of FT on the visual properties of FT-based packaging materials. On the other hand, the recycled magnetic plastics are not usable in each application. Furthermore, the side effects of the FT-based nanocomposite on ecosystem should investigate.

Supplementary Information The online version contains supplementary material available at https://doi.org/10.1007/s11356-022-22049-1.

Acknowledgements The authors would like to acknowledge Amin Babaei-Ghazvini for his remarkable suggestions and English revision of the manuscript.

Author contribution Iman Shahabi-Ghahfarrokhi contributed to the study conception and design. Material preparation, data collection, and analysis were performed by Masoumeh Mohammadi-Alamuti, Iman Shahabi-Ghahfarrokhi, and Maryam Shaterian. The first draft of the manuscript was written by Masoumeh Mohammadi-Alamuti, and all authors commented on previous versions of the manuscript. All authors read and approved the final manuscript.

Funding Masoumeh Mohammadi-Alamuti and Iman Shahabi-Ghahfarrokhi have received research funding from the Ministry of Science, Research and Technology (IRI), University of Zanjan, and Zanjan Science and Technology Park under grant number 15-00-01-000945. Iman Shahabi-Ghahfarrokhi and University of Zanjan are filling a patent regard to the results of this research project.

Data availability Video 1 illustrates the performance of the prepared magnetic biocomposite as a novel approach to auto-recycling the plastic goods.

Declarations

Ethics approval We declare that all ethical guidelines for authors have been followed by all authors.

Consent to participate All authors have given their consent to participate in submitting this manuscript to this journal.

Consent to publish Written consent was sought from each author to publish the manuscript.

Conflict of interest The authors declare no competing interests.

References

Ali SS, Qazi IA, Arshad M, Khan Z, Voice TC, Mehmood CT (2016) Photocatalytic degradation of low density polyethylene (LDPE) films using titania nanotubes. Environ Nanotechnol Monitor Manag 5:44–53

Almasi H, Ghanbarzadeh B, Entezami AA (2010) Physicochemical properties of starch–CMC–nanoclay biodegradable films. Int J Biol Macromol 46:1–5

Annonymous (2012) Solar and ultraviolet radiation. Radiation Annonymous (2021) Plastic- the Facts 2021 An analysis of Europen plastics production, demand and waste data. PLASTIC EUROPE Enabling a sustainable future

Anonymous (2018) An analysis of European plastics production, demand and waste data. Plastics – the Facts 2018

B Arkles (2006) Hydrophobicity Hydrophilicity and Silanes. Gelest Inc.: Morrisville

Arruebo M, Fernández-Pacheco R, Ibarra MR, Santamaría J (2007) Magnetic nanoparticles for drug delivery. Nano Today 2:22–32

Ashter SA (2016) Overview of biodegradable polymers. Introduction to Bioplastics Engineering 1st Edition, 19–30

ASTM (1995) Annual book of ASTM. American Society for Testing and Materials: Philadelphia, E96–E95.

ASTM (2002) Annual book of ASTM. American Society for Testing and Materials: Philadelphia, D882–D902

Babaei-Ghazvini A, Shahabi-Ghahfarrokhi I, Goudarzi V (2018) Preparation of UV-protective starch/kefiran/ZnO nanocomposite as a packaging film: characterization. Food Packag Shelf Life 16:103–111

Billings S, Li Y, Goodrich W 2009: Advanced UXO discrimination using magnetometry: understanding remanent magnetization, SKY RESEARCH INC ASHLAND OR

Bohdanecky M, Kavar J (1982) Viscosity of polymer solutions. Polymer Science Library 2/AD Jenkins (ed.)

Briassoulis D, Aristopoulou A, Bonora M, Verlodt I (2004) Degradation characterisation of agricultural low-density polyethylene films. Biosys Eng 88:131–143

Carneiro J, Teixeira V, Portinha A, Magalhaes A, Coutinho P, Tavares C, Newton R (2007) Iron-doped photocatalytic TiO2 sputtered coatings on plastics for self-cleaning applications. Mater Sci Eng, B 138:144–150

Caseri W (2010) Color switching in nanocomposites comprising inorganic nanoparticles dispersed in a polymer matrix. J Mater Chem 20:5582–5592

Cassie A, Baxter S (1944) Wettability of porous surfaces. Trans Faraday Soc 40:546–551

Chau T, Bruckard W, Koh P, Nguyen A (2009) A review of factors that affect contact angle and implications for flotation practice. Adv Coll Interface Sci 150:106–115

Chen X-Q, Zhang H-X, Shen W-H (2018) Preparation and characterization of the magnetic Fe3O4@ TiO2 nanocomposite with the in-situ synthesis coating method. Mater Chem Phys 216:496–501

Cho S, Choi W (2001) Solid-phase photocatalytic degradation of PVC–TiO2 polymer composites. J Photochem Photobiol, A 143:221–228

Ding D, Yan X, Zhang X, He Q, Qiu B, Jiang D, Wei H, Guo J, Umar A, Sun L (2015) Preparation and enhanced properties of Fe3O4 nanoparticles reinforced polyimide nanocomposites. Superlattices Microstruct 85:305–320

Djekic I, Vunduk J, Tomašević I, Kozarski M, Petrovic P, Niksic M, Pudja P, Klaus A (2017) Application of quality function deployment on shelf-life analysis of Agaricus bisporus Portobello. LWT 78:82–89

Dresselhaus M (1999) Solid state physics part iii magnetic properties of solids. Massachusetts Institute of Technology

Gaikwad KK (2015) Water vapour permeability of packaging materials (LDPE) and fabricated package systems. MS: Packaging, School of Packaging Michigan State University, East Lansing

George S, Pokhrel S, Ji Z, Henderson BL, Xia T, Li L, Zink JI, Nel AE, Mädler L (2011) Role of Fe doping in tuning the band gap of TiO2 for the photo-oxidation-induced cytotoxicity paradigm. J Am Chem Soc 133:11270–11278

Ghanbarzadeh B, Almasi H, Entezami AA (2010) Physical properties of edible modified starch/carboxymethyl cellulose films. Innov Food Sci Emerg Technol 11:697–702

Goudarzi V, Shahabi-Ghahfarrokhi I, Babaei-Ghazvini A (2017) Preparation of ecofriendly UV-protective food packaging material by starch/TiO2 bio-nanocomposite: characterization. Int J Biol Macromol 95:306–313

Goudarzi V, Shahabi-Ghahfarrokhi I (2018) Photo-producible and photo-degradable starch/TiO2 bionanocomposite as a food packaging material: development and characterization. Int J Biol Macromol 106:661–669

Graham T, Tessler J, Orris P, Shimek J, Wilson M, Witt H (2015) Protecting workers who protect the planet. Sustain Safe Recycl

Hassannia-Kolaee M, Khodaiyan F, Shahabi-Ghahfarrokhi I (2016) Modification of functional properties of pullulan–whey protein bionanocomposite films with nanoclay. J Food Sci Technol 53:1294–1302

ISO (2019) ISO 1183–1:2019 Plastics — Methods for determining the density of non-cellular plastics — Part 1: Immersion method, liquid pycnometer method and titration method

Jamróz E, Kulawik P, Kopel P (2019) The effect of nanofillers on the functional properties of biopolymer-based films: A review. Polymers 11:675

Kim I, Viswanathan K, Kasi G, Sadeghi K, Thanakkasaranee S, Seo J (2019) Poly (lactic acid)/ZnO bionanocomposite films with positively charged ZnO as potential antimicrobial food packaging materials. Polymers 11:1427

Koysuren O, Koysuren HN (2018) Photocatalytic activity of polyvinyl borate/titanium dioxide composites for UV light degradation of organic pollutants. J Macromolec Sci A 55:401–407

Kristo E, Biliaderis CG (2007) Physical properties of starch nanocrystal-reinforced pullulan films. Carbohyd Polym 68:146–158

Lee S-Y, Park S-J (2013) TiO2 photocatalyst for water treatment applications. J Ind Eng Chem 19:1761–1769

Müller CM, Laurindo JB, Yamashita F (2011) Effect of nanoclay incorporation method on mechanical and water vapor barrier properties of starch-based films. Ind Crops Prod 33:605–610

Nakayama N, Hayashi T (2007) Preparation and characterization of poly (l-lactic acid)/TiO2 nanoparticle nanocomposite films with high transparency and efficient photodegradability. Polym Degrad Stab 92:1255–1264

Nayak BB (2006) Magnetic Nanocomposite Material. PhD thesis National institute of technology Rourkela

Omrani G, Maleki A, Zmanzadeh M, Soltandalal M (2005) Plastic Recycling Problems and it's Health Aspects in Tehran. J Appl Sci 5:351–356

Rosmiati V (2020): Life cycle assessment and energy efficiency from industry of plastic waste recycling, E3S Web of Conferences. EDP Sciences, pp. 06015

Salarbashi D, Mortazavi SA, Noghabi MS, Bazzaz BSF, Sedaghat N, Ramezani M, Shahabi-Ghahfarrokhi I (2016) Development of new active packaging film made from a soluble soybean polysaccharide incorporating ZnO nanoparticles. Carbohyd Polym 140:220–227

Salarbashi D, Noghabi MS, Bazzaz BSF, Shahabi-Ghahfarrokhi I, Jafari B, Ahmadi R (2017) Eco-friendly soluble soybean polysaccharide/nanoclay Na+ bionanocomposite: Properties and characterization. Carbohyd Polym 169:524–532

Seo K, Kim M (2015) Re-derivation of Young's equation, Wenzel equation, and Cassie-Baxter equation based on energy minimization, Surface energy. InTechOpen

Seymour RB (1989) Polymer science before and after 1899: notable developments during the lifetime of Maurits Dekker. J Macromolec Sci – Chem 26:1023–1032

Shahabi-Ghahfarrokhi I, Khodaiyan F, Mousavi M, Yousefi H (2015a) Effect of γ-irradiation on the physical and mechanical properties of kefiran biopolymer film. Int J Biol Macromol 74:343–350

Shahabi-Ghahfarrokhi I, Khodaiyan F, Mousavi M, Yousefi H (2015b) Green bionanocomposite based on kefiran and cellulose nanocrystals produced from beer industrial residues. Int J Biol Macromol 77:85–91

Shahabi-Ghahfarrokhi I, Khodaiyan F, Mousavi M, Yousefi H (2015c) Preparation of UV-protective kefiran/nano-ZnO nanocomposites: Physical and mechanical properties. Int J Biol Macromol 72:41–46

Shahabi-Ghahfarrokhi I, Babaei-Ghazvini A (2019) Using photo-modification to compatibilize nano-ZnO in development of starch-kefiran-ZnO green nanocomposite as food packaging material. Int J Biol Macromol 124:922–930

Shahabi-Ghahfarrokhi I, Almasi H, Babaei-Ghazvini A (2020) Characteristics of biopolymers from natural resources. In: Zhang Y (ed) Processing and development of polysaccharide-based biopolymers for packaging applications, 1st edn. CRC Press, Alberta, pp 49–95

Shrivastava A (2018) Plastic properties and testing. In: Introduction to Plastics Engineering, William Andrew Publishing, pp 49–110

Thompson R, Oldfield F (1986) Magnetic properties of solids. Environmental Magnetism. Springer, Dordrecht, pp 3–12

Tian H, Yan J, Rajulu AV, Xiang A, Luo X (2017) Fabrication and properties of polyvinyl alcohol/starch blend films: Effect of composition and humidity. Int J Biol Macromol 96:518–523

Tran T, Da G, Moreno-Santander MA, Vélez-Hernández GA, Giraldo-Toro A, Piyachomkwan K, Sriroth K, Dufour D (2015) A comparison of energy use, water use and carbon footprint of cassava starch production in Thailand, Vietnam and Colombia. Resour Conserv Recycl 100:31–40

Tu-morn M, Pairoh N, Sutapun W, Trongsatitkul T (2019) Effects of titanium dioxide nanoparticle on enhancing degradation of polylactic acid/low density polyethylene blend films. Materials Today: Proceedings 17:2048–2061

Wang F, Zhang K (2011) Reduced graphene oxide–TiO2 nanocomposite with high photocatalystic activity for the degradation of rhodamine B. J Mol Catal a: Chem 345:101–107

Wenzel RN (1936) Resistance of solid surfaces to wetting by water. Ind Eng Chem 28:988–994

Xing M, Qiu B, Li X, Zhang J (2016) TiO2/Graphene composites with excellent performance in photocatalysis. In: Yamashita H, Li H (eds) Nanostructured photocatalysts. Springer, Switzerland, pp 23–67

Xu J-K, Zhang F-F, Sun J-J, Sheng J, Wang F, Sun M (2014a) Bio and nanomaterials based on Fe3O4. Molecules 19:21506–21528

Xu J, Sun J, Wang Y, Sheng J, Wang F, Sun M (2014b) Application of iron magnetic nanoparticles in protein immobilization. Molecules 19:11465–11486

Yousif E, Haddad R (2013) Photodegradation and photostabilization of polymers, especially polystyrene. Springerplus 2:1–32

Zan L, Fa W, Wang S (2006) Novel photodegradable low-density polyethylene− TiO2 nanocomposite film. Environ Sci Technol 40:1681–1685

Zhou J, Wang S, Gunasekaran S (2009) Preparation and characterization of whey protein film incorporated with TiO2 nanoparticles. J Food Sci 74:N50–N56

Zolfi M, Khodaiyan F, Mousavi M, Hashemi M (2014) Development and characterization of the kefiran-whey protein isolate-TiO2 nanocomposite films. Int J Biol Macromol 65:340–345